Nanodomain fragmentation and local rearrangements in CdSe under pressure

Stefano Leoni[1], Reiner Ramlau, Katrin Meier, Marcus Schmidt, and Ulrich Schwarz

Max-Planck-Institut für Chemische Physik fester Stoffe, Nöthnitzer Strasse 40, 01187 Dresden, Germany

Edited by E. Ward Plummer, University of Tennessee, Knoxville, TN, and approved October 29, 2008 (received for review May 30, 2008)

Structural transformations in extended solids result from local atomic rearrangements and phase growth mechanisms. A broad class of technologically relevant properties critically depends on local structural issues connected with domain sizes, domain boundary geometries, and defects. However, a precise understanding of structural transformation mechanisms and domain formation is still an open question. Here, we demonstrate the feasibility of very detailed mechanistic investigations in real materials as a prerequisite for intelligent property control. We address the problem of domain fragmentation in bulk CdSe under pressure, jointly by molecular dynamics simulations, high-pressure experiments, and HR-TEM imaging. We show that domain fragmentation is taking place in the high-pressure regime, where nucleation events generate both zinc blende (B3) and wurtzite (B4) structural motifs and, in turn, cause the final lamellar appearance observable by high-resolution TEM. A changed nucleation pattern and a modified B3/B4 ratio represents the system's response to modified external stress conditions.

domains | metastable phases | molecular dynamics | polymorphism | solid–solid phase transition

Recent challenges posed to solid-state sciences in terms of discovery of novel materials and tailoring of properties has made a rational approach to material reactivity and structural polymorphism a task of top priority (1–7). To control properties as diverse as mechanical stability or hardness (8, 9), ferroelectric response (10), and conductivity switching (11), even mass and electron transport properties in general (12, 13), a precise knowledge of atomistic processes in the stadium of phase formation is necessary. Although for a given composition the ground state structures can typically be assigned by theory, the understanding of intermediate, metastable geometries and the prediction of their occurrence implies shedding light on transformation mechanisms between different atomic configurations. Gathering evidence for such mechanisms is an intrinsically difficult task, which in real solids may be further complicated by multidomain scenarios and by high defect concentrations. For this reason, investigations on the kinetics of first-order structural transition have recently turned to nanocrystals as prototypes for single-domain phase transformation (7, 14). Therein, the action of a particular mechanism is mapped onto a characteristic, observable change of shape of the nanocrystals. However, a precise atomistic understanding of mechanisms and domain formation and further a reliable extrapolation from nano to bulk material are still open issues.

Capturing the complex kinetics of structural transformations from theoretical simulations entails working out an atomistic landscape that allows for a detailed understanding of local structural rearrangements. Recently, we have shown that molecular dynamics (MD) simulations and modeling comprise suitable tools for performing detailed investigations of reconstructive phase transitions at experimental conditions, with a resolution and on a time scale that are still inaccessible to experiments (15–17).

Here, we describe the evolution of domain morphologies and shape in bulk CdSe under the effect of pressure, both from theory and experiment. We are interested in studying the mechanisms and length scales of solid–solid transformations, their scaling properties compared with single-domain kinetics in nanocrystals, and the transferability of mechanistic models from nanocrystals to bulk materials. The mechanistic issues of CdSe transformation have been an open problem for many decades (18–29). In experiments on CdSe and ZnO nanocrystals, structural transformations are traced back to a single nucleation event and to simplest kinetics (7, 20, 21). On monitoring shape changes, the activation volume can be directly investigated and mechanisms involved in the phase transformation can be suggested (7).

CdSe is a wide-gap semiconductor that has found extensive use in optical applications for its rich set of effects in the nanoregime. Under normal conditions, it crystallizes in the wurtzite structure type (B4). Applying moderate pressure (2.5–3.5 GPa) it transforms into the rock-salt structure type (B1) (18). As a third polymorph, zinc blende (B3 structure type), albeit metastable, does exist. Evidence of possible coexistence of structural motifs of B3 and B4 has been collected from experiments on nanocrystals (20, 21), bulk CdSe (19), and from mechanically manipulating samples with B4 arrangement (23). Irregularities in resistivity measurements may reflect a changed stacking sequence (24). Pair-distribution function analysis (PDF) also concludes on stacking faults in nano and bulk crystals (25). However, no insight into the atomistic origin of such coexistence has been proposed. Rather, model mechanisms of B3 $\rightarrow$ B1 (26) or of B4 $\rightarrow$ B1 (18, 19, 27) transformations are often considered. A combination of B4 and B3 regions in a single material represents a means of achieving the most simple domain boundaries without locally discontinuing the lattice or introducing vacancies. Nonetheless, whereas first-principle calculations conclude the energetic closeness of the B4 and B3, B4 represents the ground state structure (28). Here, we recast the issue in a more general context and pose the question: What qualifies a certain configuration as (meta)stable under variation of a thermodynamic parameter, e.g., pressure? Along this line the formation of a final morphology at given conditions shall be investigated as a result of the transformation of a high pressure polymorph, B1, in this case. In bridging the gap between ab initio phase stability assessment and experimental investigation, the molecular dynamics-based approach used in the following provides the necessary time resolution to capture nucleation and growth phenomena, required for reconciling many aspects of polymorphism.

Results and Discussion

Crystals of CdSe were synthesized by chemical vapor transport as a means to achieve very low defect concentrations. EDXS and X-ray powder diffraction (XRPD) verified purity and quality of the probe. Several high-pressure experiments were performed in the range 0.0001–7.9 GPa. Transformation to B1 was monitored by in situ XRPD in standard and high-resolution experiments,

Author contributions: S.L. designed research; S.L., R.R., K.M., M.S., and U.S. performed research; S.L. and R.R. analyzed data; and S.L. wrote the paper.

The authors declare no conflict of interest.

This article is a PNAS Direct Submission.

Freely available online through the PNAS open access option.

[1]To whom correspondence should be addressed. E-mail: leoni@cpfs.mpg.de.

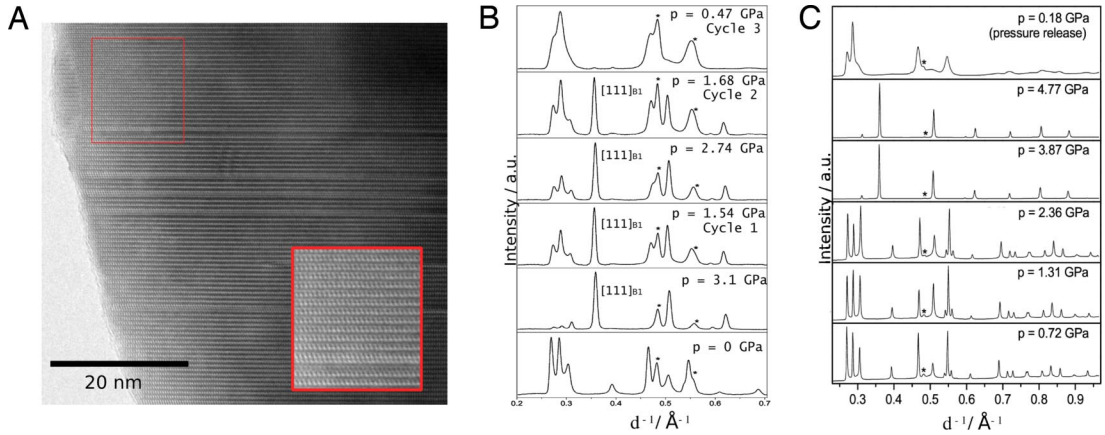

Fig. 1. B1-B4-B3 phase coexistence under pressure. (*A*) HR-TEM before sample pressurization. Large domains (≈20 nm) separated by lamellar insets are visible. The wurztize pattern is enlarged in the framed *Inset*. (*B*) X-ray powder diffraction collected in situ during 3 pressurization cycles. In regions of phase coexistence between $P = 1.5$ and $P = 3.1$ GPa signal coarsening is indicative of domain fragmentation. (*C*) X-ray powder diffraction from in situ synchrotron measurements during a single pressurization run up to 4.77 GPa followed by pressure release. Notice the loss of signal structuring. Reflection lines marked with stars are due to the metal gasket of the diamond cell.

the latter using synchrotron radiation. Subsequently, the material was gathered and prepared for HR-TEM investigation.

In Fig. 1*A*, a HR-TEM image of the starting material is displayed. Therein, extensive wurtzite-type domains are visible with tiny lamellar insets. The latter may be ascribed to mechanical manipulation during sample preparation (23). X-ray powder diffraction measurements collected during 3 pressurization/depressurization cycles are displayed in Fig. 1*B*. A progressive coarsening indicative of overall domain size reduction takes place at intermediate pressures between 1.54 and 3.1 GPa, in regions of phase coexistence. In Fig. 1*C* a set of powder diffraction diagrams taken during a single compression run is presented. Complete transformation of the starting material into B1 is achieved >3.5 GPa, with a hysteresis offset of ≈1 GPa with respect to equilibrium pressure (29).

Upon release of pressure, the appearance of the diffraction pattern is remarkably different from the starting one. A broadening of the peaks, as well as a strong perturbation of the relative line intensities is evident especially in the manifold ≈0.3 reciprocal lengths (Fig. 1 *B* and *C*). Such a pattern is characteristic of the final product, and a slower decompression or a different pressurization profile does not appreciably alter it. This suggests a lower limit for domain fragmentation. The initial 4-connected B4 material is thus very different from the final product. This hints at a structurally diverse scenario of (sub)nanodomains that originate in the high-pressure regime.

To elucidate the formation of domains under pressure and to back-trace domain fragmentation to nucleation events, we have performed transition path sampling (TPS) (30) MD simulations on the B4–B1 reconstructive phase transition. This particular flavor of trajectory sampling implements an iterative optimization process of an initial dynamical trajectory toward a stable regime, with distinctive features (see *Materials and Methods* for details).

Although any initial trajectory connecting B4 to B1 can, in principle, be considered, we have used a geometric model connecting B3 and B1, bypassing B4 on purpose. This strategy corresponds to starting the simulation in a regime delimited by metastable modifications, B1 and B3, and converging the simulation runs toward a stable regime. Such an approach has the advantages of (*i*) an enhanced performance in the calculation, because the initial regime is expected to be very unfavorable and (*ii*) a clear tracing of the role of B3 and B4 structures during phase formation, obtained by subsequent trajectory refinement (see *Materials and Methods*), from a *gedankenexperiment* to a realistic transformation.

Fig. 2 displays the initial mechanism connecting B3 to B1 and the trajectory evolution toward the final configurations (a representative configuration is displayed here) after convergence. A contraction along c ($[0001]_{B4}$,$[111]_{B1}$) is hardly significant, in contrast to the initial mechanism, and in agreement with experiments (19, 21). We notice the intertwined B3/B4 motifs.

An analysis on the mechanistic details was performed to shed light on the origin of the lamellar arrangement. Fig. 3 shows 5 snapshots of a representative trajectory. In the B1 structure matrix (Fig. 3*A*) initial nuclei of B4 type pattern start to form (Fig. 3*B*, purple circles), followed by regions of B3 structural motifs (Fig. 3*C*, yellow circle), which grow between already defined B4 regions in a more confined region of space. Notice the dominance of B4 regions at this point. The final (sub)nanodomains result from further growth of this initial configuration (Fig. 3*E*). No domain recombination is observed during growth. Instead, both B3 and B4 originate from the B1 structure and do not imply intralayer

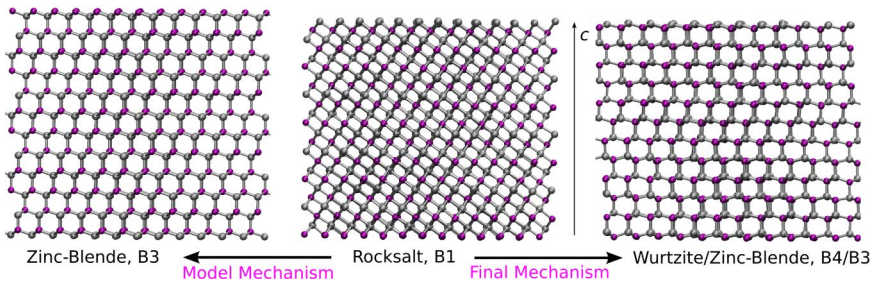

Fig. 2. Mechanism model and final mechanistic regime from MD simulations. Evolution of MD simulation runs from an initial mechanism connecting B3 and B1 (*Left*) toward a final regime (*Right*) characterized by lamellar insets of B3 structural motifs.

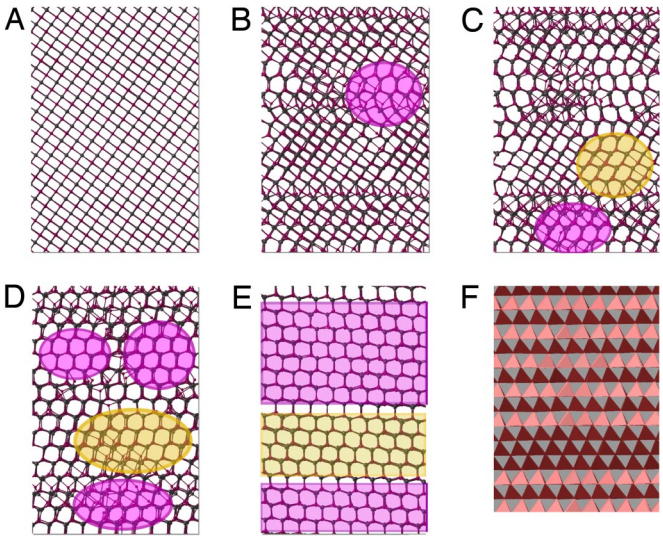

Fig. 3. Nucleation and growth of B3 and B4 domains under pressure. (*A*) Initial B1 configuration. (*B–D*) Nucleation of B4 (purple) and B3 (yellow) motifs, respectively. (*E*) Final lamellar arrangement. (*F*) Polyhedral representation highlighting the lamellar B3 inset (dark red) within B4 (bright red).

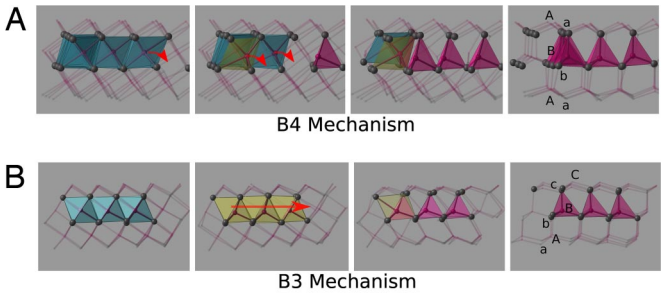

Fig. 4. Diffusive and displacive mechanisms in CdSe lattice reconstruction. (*Upper*) Diffusive mechanism characterizing the growth of B4 regions (B4 Mechanism). (*Lower*) Displacive character connected to the growth of B3 regions (B3 Mechanism).

rearrangements. Intermediate patchwork configurations of B1, B3, B4 (Fig. 3 *C* and *D*) characterize the later transformation stages and slow down the nonetheless complete transformation to the final void-free 4-connected structural motif (Fig. 3*E*). In Fig. 3*F*, the coordination of Cd by Se is represented by way of polyhedra. Three-layer lamellae of B3 phase are clearly visible between more extended B4 regions. This lamellar structure in which wurtzite is the dominating component (1/4 B3 to 3/4 B4, on average) is typical for the lower pressure range inside the hysteresis, here at $P = 2.5$ GPa. In this region, our simulations are able to provide detailed atomistic insights into the phase coexistence, which is otherwise difficult to experimentally determine in this regime.

The local nucleation events leading to B3 and B4 structural motifs subsume distinctive mechanistic pattern. Three-layered regions that grow into B4 and B3 domains are shown in Fig. 4 *A* and *B*, respectively. The final layer sequence aAbBaA—distinctive of the hexagonal stacking of B4—is formed by displacing Cd cations between Se layers (Fig. 4, B4 Mechanism) whereby only 3 of the initially 6 Se remain in the next-neighbor (n-n) coordination sphere of Cd. For B3 (Fig. 4*B*) with cubic layer sequence aAbBcC, Cd is shifted in a similar manner but does conserve 4 of the initial 6 Se atoms in its n-n coordination sphere (B3 mechanism). Both types of displacements take place within (001) layers perpendicular to $[0001]_{B4}$ of the final wurtzite regions. They contain a diffusive and a displacive component, the former being more pronounced in the B4 mechanism, whereas the latter is more pertinent in the B3 mechanism. With reference to Figs. 3 and 4, the B3 formation appears more martensitic-like, possibly reflecting the confined growth condition. Their alternation suggests a tendency to locally minimize strain, which would be very large in case of a complete layer sliding. Accordingly, different regions may respond to changed external pressures in different ways. We recall that the condition for the formation of B3 and B4 appeared to be different, B4 characterizing the initial formation stage and B3 being more connected to the mature growth of the material.

To better understand the role of local transformation pattern and morphology changes, a set of simulations was performed for nominal pressures in the range of $P = 3.5$–3.8 GPa, i.e., in the upper part of the hysteresis regime (see Fig. 1*C*). HR-TEM investigations were independently performed on samples pressurized within or slightly above the simulation range, and the results were compared regarding common features, that is, with respect to domain structuring.

Here, we have to point out that diverse effects have to be expected because of sample preparation. Apart from mechanical loading due to sample manipulation, the requirement of electron-beam sample transparency does de facto privilege boundary regions of the samples. Nonetheless, the atomistic origin of domain structure and its connection to distinct nucleation events—as it has appeared from simulations at lower pressures—should not be obscured by accident. With this caveat in mind, we now proceed to present the simulation results in relation to HR-TEM images.

The final configurations obtained from TPS-MD simulations display a scenario of alternating B4 and B3 structural motifs, in analogy to what was observed in the lower-pressure simulations. However, B3 lamellae are more frequent, and their thickness is variable. Two configurations resulting from different simulation runs are displayed in Fig. 5 *A* and *B*.

In going from lower (Fig. 5*B*, $P = 3.5$ GPa) to slightly higher pressure (Fig. 5*C*, $P = 3.8$ GPa) the ratio of amount of B3 lamellae to B4 ones increases, from B3/B4 $\simeq 0.8$ to B3/B4 $\simeq 1.0$, with B3 and B4 layer thicknesses becoming similar (Fig. 5*B*). In the HR-TEM image of Fig. 5*A*, a lamellar structure is apparent, with alternating B3 lamellae of different thickness involving 3–5 layers. Here, we present 2 images from different samples exposed to different loadings. The sample boundaries are typically dominated by B3 structure motifs. In Fig. 5*D*, a lamellar arrangement with a dominating internal region of B3 structure is shown. Both simulations and HR-TEM sample investigations do agree on the features, that is (*i*) a lamellar appearance of the sample and stacking direction and (*ii*) a size and distribution variation of lamellae, with a pronounced role of B3 on increasing pressure.

Owing to the difference in the mechanisms connected to nucleating B3 or B4 patterns, their response to pressure increase is also different. B3 regions grow faster on average but not as a consequence of an enhanced single-domain growth kinetics. Rather, this reflects a change in the nucleation pattern as an increment in the number of events leading to B3 domains. Although at lower pressure ($P = 2.5$ GPa) already 1/2 of the final B4 regions have formed at the time of the onset of B3 nucleation, at higher pressure ($P = 3.5$ GPa) only 1/3 of B4 is formed before B3 starts growing. B4 also grows from many tiny lamellae propagating from as many nucleation centers. On average, B3 growth is thus enhanced under pressure. Analogous to nanocrystals (21, 22) individual domains in the bulk (B3 or B4) are connected to distinct generating events. In contrast to nanocrystals, a nucleation pattern rather than a single nucleation event promotes the phase transformation (see Fig. 3). The lamellar appearance of the resulting material and the broadening of the diffraction lines result from local rearrangements (B3 and B4 mechanisms), nucleation center density and domain growth.

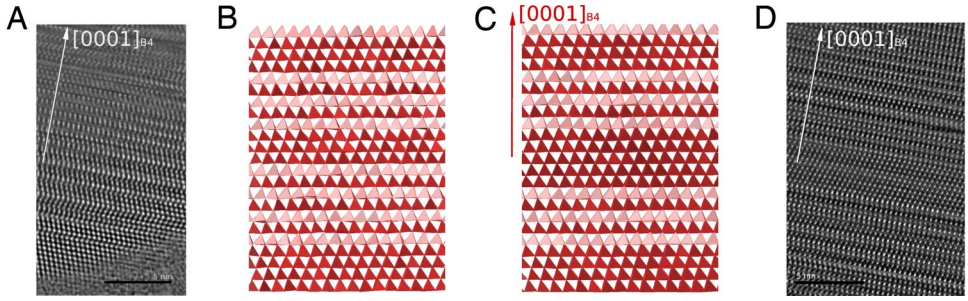

Fig. 5. Lamellar domains of intertwined B3 and B4 motifs. (*A*) HR-TEM images of lamellar domains on pressurized samples. (*B* and *C*) Final configuration from MD simulations in the high-pressure regime between $P = 3.5$ GPa and $P = 3.8$ GPa. (*D*) HR-TEM images of another sample with larger domains of the B3 structural motif.

Another manifestation of local rearrangements under pressure is the formation of a different type of defects. We have shown that lamellar domains of B3 are separated by B4 lamellae. Additionally, within a B3 domain, skew 3-layer insets of B4 structural motifs can be formed. As for the previous defects, this does not require introducing vacancies in the lattice, as is apparent from Fig. 6 *B* and *C*. In the polyhedra representation (Fig. 6*B*) local distortions are visible that reflect distorted 6-membered rings (Fig. 6*C*). This type of defect can be recognized in the HR-TEM image of Fig. 6*A*. An *Inset* of the B4 motif is visible separating regions within a B3 domain and terminating inside a B4 domain. Within the B4 region the defect does not cause any dislocation in the atomic pattern (see Fig. 6 *A*–*C*), because the incidence angle with the (001) planes of ≈70° is preserved. Only locally, at the acute-angled intersection of stacking fault onset and defect, changes are clearly visible as distorted 6-membered rings. Even if the size of the simulation system is small compared with the number of atoms inside the sample, the feature is precisely identified. Furthermore, the simulation augments the HR-TEM image by a detailed atomistic picture, not only on the local geometry, but also on the very origin of the defect that is rooted in the local transformation pattern of CdSe under pressure.

In single-crystal X-ray diffraction experiments, crystal integrity is often compromised due to strain. Nonetheless, preferential orientations of the final microcrystals with respect to the initial matrix can be investigated, which are often used to support mechanistic models. In a recent work (19) tilting angles of ≈5° between final B1 ⟨100⟩ planes and B4 [0001] have been reported. Additionally, deviations within (001) appear. Our simulations and experiments support a correspondence between B1 [111] and B4 [0001], consistent with experiments on compressing nanocrystals (21) and constant-pressure simulations (26). Nonetheless, the skew defects introduce a reorientation of B4 planes perpendicular to [0001] that forms an angle of ≈5° with B1 [001] (see Fig. 6 *C* and *D*). It is fascinating to observe how different direction (mis)alignments can be accommodated in the same vacancy-free 4-connected lattice without invoking a scenario of a severely mechanically perturbed sample. A different lattice alignment between initial and final structures has typically been used to support or to exclude a particular mechanism. Here, we infer that this rule may result in too-stringent conclusions. On the contrary, looking at the nucleation pattern under pressure as a source of defect formation may offer a more appropriate approach to the comprehension of structural transformations (31).

Previous works based on crystallographic/geometric models assumed collective displacements of atoms for the transition (32). Although such models may help in the interpretation of preferential orientations to some extent, the assumption of cooperativeness in the atomic motion does not allow to capture domain and defect formation, because local nucleation phenomena are elusive to the models. On the contrary, our approach allows simulations to be performed at pressures corresponding to experimental values, free of any assumption on atomic displacements during the transition. This allows for the identification of nucleation events as key ingredients for understanding domain formation and domain fragmentation. Distinct local rearrangements are responsible for the formation of B3 and B4 regions, which do grow next to each other into the final material. The alignment of the stacking direction of B3 motifs with B1 [111] is consistent with previous constant-pressure simulations (26). Additionally, we show how local mechanisms can accommodate different motifs along the same stacking direction without voids, by clearly tracing back mature domains to their distinct generating events. The domain morphogenesis dis-

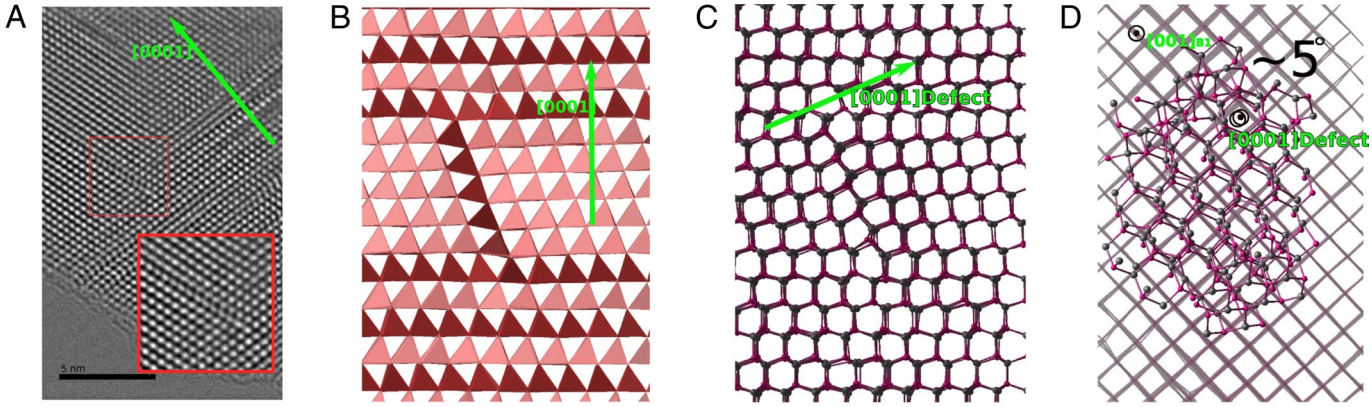

Fig. 6. Defect formation under pressure and lattice reorientation. (*A*) HR-TEM image of defects, magnified in the *Inset*. (*B* and *C*) Defects of B4 structural motifs from MD simulations. The [0001] direction of the B4 defect is indicated. (*D*) Alignment of [0001] of the B4 defect with respect to the initial [001] of the B1 structure. An offset of ≈5° is visible.

covered along this line of study matches HR-TEM maps of the transformed material.

Conclusions

In summary, we have performed high-pressure experiments and MD simulations on the B1-(B4,B3) pressure-induced transformation. A distinct rearrangement pattern underlying local mechanisms has emerged that causes B4 and B3 lamellar domains to form on releasing pressure from B1 transformed samples. The features emerging from the simulations compare very well with HR-TEM images. Altogether, a precise atomistic picture from theory and experiments, which allows us to reconcile many experimental observations, has emerged.

Materials and Methods

Synthesis. Crystals of CdSe ($1 \times 1 \times 4$ mm) were grown from microcrystalline powder by chemical vapor transport using iodine as a transport agent. The endothermal transport reaction took place in a temperature gradient from 1,073 K (source) to 973 K (sink). The transport condition was derived from thermodynamic data and from DTA/TG (differential thermo-analysis) measurements.

High-Pressure. High-pressure investigations were performed by using the diamond anvil cell (DAC) technique with 4:1 mixtures of methanol and ethanol as pressure-transmitting medium. Pressure was measured by the ruby luminescence method (33, 34).

High-pressure X-ray diffraction experiments were performed in situ by using DACs with beryllium backing plates allowing for the recording of complete diffraction rings. The diffractometer was operated with Zr-filtered Mo K_a radiation collimated to a beam size of 0.125 mm, intensities were recorded with an imaging plate ($\lambda = 70.93$ pm, graphite monochromator). All structure refinements were performed with the WinCSD program package. For high-resolution powder diagrams at selected pressures, we used synchrotron radiation ($\lambda = 41.3122$ pm) at beamline ID09A of the European Synchrotron Radiation Facility.

Electron Microscopy. HR-TEM was performed with a FEI Tecnai G2-F30 electron microscope ($C_S = 1.2$ mm) operated at 300 kV, equipped with a Gatan GIF2001 imaging filter and a Gatan UltraScan 1000 charge-coupled device camera. The samples were ground in an agate mortar, dispersed in 1-butanol and spread over a holey carbon film. HR-TEM defocus-series of CdSe samples were recorded for zone axes orthogonal to [0001].

MD Simulations. TPS-MD (30) iterations within the NpT ensemble were implemented by applying momentum modifications on selected trajectory snapshots, keeping total energy, momentum, and angular momentum unchanged (15). Propagating the new configuration in both directions in time provides a new trajectory that is examined for the B1 $\rightarrow$ (B4,B3) or (B4,B3) $\rightarrow$ B1 process, respectively. Iterations are performed until trajectory convergence (characterized by stable mechanistic features) is reached. The simulation scheme requires a model trajectory connecting the limiting structures. Here, we have commenced the simulation from a path connecting B3 to B1, obtained from a geometric-topological approach, based on transforming minimal surfaces (35, 36). The classical MD simulations were carried out by using the DLPOLY package (37). The CdSe pair potential of Rabani was used (29, 38). A relatively small simulation time step of 0.15 fs was used to ensure a good time-reversibility. The Melchionna/Nose-Hoover algorithm (39) ensured constant pressure and temperature. Therein, anisotropic shape changes of the simulation box were allowed. Different simulation sets were performed in the pressure range 2.5–3.8 GPa, at 300 K. In the course of iterations, the collective characteristics of the geometric model disappeared, and a regime characterized by nucleation and growth set in. The mechanistic analysis is based on >200 transition pathways for each pressure value, collected after trajectory convergence.

ACKNOWLEDGMENTS. We thank Dirk Zahn, Juri Grin, Rüdiger Kniep, Gotthard Seifert, Luis Craco, and Ulrich Burkhardt for comments and discussions. S.L. thanks Hartmut Bärnighausen and Ulrich Müller for deep insights into the domain problematic, and Michele Parrinello for stimulating discussions. Francesco Mercuri, Salah Eddine Boulfelfel, Marek Pasciak, and Mukul Laad are acknowledged for comments. We thank Steffen Wirth for stylistic insights. The graphics were produced with STM4 of Mario Valle (http://personal.cscs.ch/mvalle). The computational center of the Technical University in Dresden (ZIH) and the computational center of the Max Planck Society are acknowledged for computational time. S.L. is indebted to the Max Planck Society and to the Swiss National Science Foundation for support.

1. Anonymous (2002) Our changing nature. *Nat Mater* 1:1.
2. Hart GLW (2007) Where are nature's missing structures? *Nat Mater* 6:941–945.
3. Maddox J (1988) Crystals from first principles. *Nature* 335:201.
4. Ensing B, Klein ML (2005) Perspective on the reactions between F^- and CH_3CH_2F: The free energy landscape of the E2 and S_N2 reaction channels. *Proc Natl Acad Sci USA* 102:6755–6759.
5. Laio A, Parrinello M (2002) Escaping free-energy minima. *Proc Natl Acad Sci USA* 99:12562–12566.
6. Jansen M, Schön JC (2006) ''Design'' in chemical synthesis—An illusion? *Angew Chem Int Ed* 45:3406–3412.
7. Chen C-C, Herhold AB, Johnson CS, Alivisatos AP (1997) Size dependence of structural metastability in semiconductor nanocrystals. *Science* 276:398–401.
8. Schall P, Cohen I, Weitz DA, Spaepen F (2006) Visualizing dislocation nucleation by indenting colloidal crystals. *Nature* 440:319–323.
9. Jacobsen KW, Schiotz J (2002) Computational materials science: Nanoscale plasticity. *Nat Mater* 1:15–16.
10. Jia C-L, *et al.* (2007) Unit-cell scale mapping of ferroelectricity and tetragonality in epitaxial ultrathin ferroelectric films. *Nat Mater* 6:64–69.
11. Szot K, Speier W, Bihlmayer G, Waser R (2006) Switching the electrical resistance of individual dislocations in single-crystalline $SrTiO_3$. *Nat Mater* 5:312–320.
12. Maier J (2005) Nanoionics: Ion transport and electrochemical storage in confined systems. *Nat Mater* 4:805–815.
13. Aricò AS, Bruce P, Scrosati B, Tarascon J-M, Van Schalkwijc W (2005) Nanostructured materials for advanced energy conversion and storage devices. *Nat Mater* 4:366–377.
14. Zaziski D, *et al.* (2004) Critical size for fracture during solid-solid phase transformations. *Nano Lett* 4:943–946.
15. Zahn D, Leoni S (2004) Nucleation and growth in pressure-induced phase transitions from molecular dynamics simulations: Mechanism of the reconstructive transformation of NaCl to the CsCl-type structure. *Phys Rev Lett* 92:250201.
16. Boulfelfel SE, Zahn D, Grin Yu, Leoni S (2007) Walking the path from B4- to B1-type structures in GaN. *Phys Rev Lett* 9:125505.
17. Leoni S (2007) Solid-solid phase transitions: Interface controlled reactivity and formation of intermediate structures. *Chem Eur J* 13:10022–10029.
18. Mariano AN, Warekois EP (1963) High pressure phases of some compounds of groups II–VI. *Science* 142:672–673.
19. Sowa H (2007) The high-pressure behaviour of CdSe up to 3 GPa and the orientation relations between its wurtzite- and NaCl-type modifications. *Solid State Sci* 7:1384–1389.
20. Tolbert SH, Alivisatos AP (1994) Size dependence of a first order solid-solid phase transition: The wurtzite to rock salt transformation in CdSe nanocrystals. *Science* 265:373–376.
21. Wickham JN, Herhold AB, Alivisatos AP (2000) Shape change as an indicator of mechanism in the high-pressure structural transformations of CdSe nanocrystals. *Phys Rev Lett* 84:923–926.
22. Grünwald M, Rabani E, Dellago C (2006) Mechanisms of the wurtzite to rocksalt transformation in CdSe nanocrystals. *Phys Rev Lett* 96:255701.
23. Geddo Lehmann A, Bionducci M, Buffa F (1998) Effect of mechanical grinding on the hexagonal structure of CdSe. *Phys Rev B* 58:5275–5281.
24. Al'fer SA, Skums VF (2001) Electrical resistance of CdSe and CdTe at elevated temperatures and pressures. *Inorg Mater* 37:1237–1240.
25. Masadeh AS, *et al.* (2007) Quantitative size-dependent structure and strain determination of CdSe nanoparticles using atomic pair distribution function analysis. *Phys Rev B* 76:115413.
26. Wilson M, Madden P (2002) Transformations between tetrahedrally and octahedrally coordinated crystals: The wurtzite $\rightarrow$ rocksalt and blende $\rightarrow$ rocksalt mechanisms. *J Phys Condens Matter* 14:4629–4643.
27. Stokes HT, *et al.* (2007) Bilayer sliding mechanism for the wurtzite-to-rocksalt transition. *Phys Rev B* 76:012012.
28. Côté M, Zakharov O, Rubio A, Cohen ML (1997) Ab initio calculations of the pressure-induced structural phase transitions for four II–VI compounds. *Phys Rev B* 55:13025–13031.
29. Rabani E (2002) An interatomic pair potential for cadmium selenide. *J Chem Phys* 116:258–262.
30. Bolhuis PG, Dellago C, Chandler, D. (1998) Sampling ensembles of deterministic transition pathways. *Faraday Discuss* 110:421–436.
31. Bärnighausen H (1970) The crystal structure of $LiEu_3O_4$ (Translated from German). *Z Anorg Allg Chem* 374:201–224.
32. Sowa H (2001) On the transition from the wurtzite to the NaCl type. *Acta Crystallogr A* 57:176–182.
33. Piermarini GJ, Block S, Barnett JD, Forman RA (1975) Calibration of the pressure dependence of the R_1 ruby fluorescence line to 195 kbar. *J Appl Phys* 46:2774–2780.
34. Mao HK, Xu J, Bell PM (1986) Calibration of the ruby pressure gage to 800 kbar under quasi-hydrostatic conditions. *J Geophys Res* 91:4673–4676.
35. Leoni S, Zahn D (2004) Putting the squeeze on NaCl: Modelling and simulation of the pressure driven B1–B2 phase transition. *Z Kristallogr* 219:339–344.
36. Leoni S, Nesper R (2000) Elucidation of simple pathways for reconstructive phase transitions using periodic equi-surface (PES) descriptors. The silica phase system. I. Quartz-tridymite. *Acta Crystallogr A* 56:383–393.
37. Smith W, Forester TJ (1996) DL_POLY_2.0 : A general-purpose parallel molecular dynamics simulation package. *J Mol Graphics* 14:136–141.
38. Zahn D, Grin Yu, Leoni S (2005) Mechanism of the pressure-induced wurtzite to rocksalt transition of CdSe. *Phys Rev B* 72:64110.
39. Melchionna S, Ciccotti G, Holian BL (1993) Hoover NPT dynamics for systems varying in shape and size. *Mol Phys* 78:533–544.